Modeling of Micro Cat's Eye Retro-Reflectors Using a Matrix-based Three-dimensional Ray Tracing Technique

Bing-jun Yang, Keng-hsing Chao, and Jui-che Tsai

Graduate Institute of Photonics and Optoelectronics and Department of Electrical Engineering, National Taiwan University, Taipei, Taiwan.

**Corresponding author: jctsai@cc.ee.ntu.edu.tw; phone: +886-2-3366-3700 Ext. 247; fax: +886-2-3366-3686*

Abstract:

In this paper we develop a three-dimensional (3D) ray tracing tool based on the ABCD ray transfer matrices. With symmetric optical components and under paraxial approximation, two sets of 2 × 2 ABCD matrices, each for a two-dimensional subspace, can be used to describe the 3D ray propagation completely. Compared to commercial ray-tracing software packages, our tool requires no tedious drawing, and the results for various conditions, such as different device dimensions and incident angles, can be easily obtained by simply changing the parameter values used for the calculation. We have employed this matrix-based 3D ray tracing tool to model cat's eye retroreflectors. The cat's eye performance, including the retroreflection efficiency, acceptance angle (i.e., field of view), and beam divergence and deviation, is fully studied. The application of this 3D ray tracing technique can be further extended to other optical components.

1. Introduction

Optical retroreflectors possess the ability to reflect light back along its incoming direction. They are already seen in many applications, ranging from the commonplace traffic signs [1] to the free-space optical communication systems built for military platforms [2-5]. Their potential of being used in an optical ID system has also been demonstrated [6-8]. There are two major types of retro-reflectors, the corner cube retro-reflector (CCR) consisting of three orthogonal mirrors, and the cat's eye retroreflector; which combines a focusing lens and a reflecting mirror.

The retro-reflection efficiency of a CCR mainly depends on the orthogonality between mirrors and the mirror curvature, and has been comprehensively analyzed [9]. The 3-dB acceptance angle, i.e. 3-dB field of view (FOV), of a hollow perfect CCR is intrinsically ~ ±10° [10]. The FOV can only be changed by filling the CCR with some non-air medium; for example, BK7 glass increases the FOV to ~ ±15° [11]. Filler materials with higher refractive indices give greater FOVs; however, they are difficult to acquire and costly.

Cat's eye retro-reflectors can exhibit better FOVs if properly designed [10], but on the other hand, evaluating the performance of a cat's eye retroreflector is more complicated as many factors such as the lens' focal length, mirror curvature, and longitudinal distance and lateral offset (misalignment) between the lens and mirror, can all play a role in the cat's eye efficiency, reflected beam's direction and divergence, and acceptance angle. Therefore, performing device simulation and analysis prior to fabrication becomes crucial, particularly for micro cat's eye manufactured with semiconductor process or the like where slight process deviation can lead to significant changes in the parameters described above.

Several commercial ray tracing software packages can be used for this purpose. However, they are mostly expensive, and the modeling, starting from drawing the device structure, tracing

the optical rays, to calculating the efficiency, are generally time-consuming. In this paper, we develop a simulation tool based on the ABCD ray transfer matrices. No drawing is required, and results for various conditions such as different device structures and incident angles can be easily obtained by simply changing the parameter values used for the calculation.

Most literature, particularly textbooks, demonstrates ray tracing with the 2×2 ABCD matrices in a two dimensional (2D) space which is defined by the propagation direction, say *z* axis, plus a transverse axis, say *x* or *y* axis [12-16]. This paper confirms that with symmetric optical components and under paraxial approximation, two sets of 2×2 ABCD matrices, each for a 2D subspace, can be used to describe the 3D ray propagation completely, and we have employed this matrix-based 3D ray tracing technique to model various cat's eye retroreflectors.

2. Ray transfer matrices

Consider a 2D space defined by the propagation direction, *z* axis, and a transverse *x* axis. An optical ray entering the entrance pupil at position *x* with slope α passes through the system and exits from the exit pupil at position *x*' with slope α'. The relation between (x, α) and (x', α') is determined by the 2×2 ABCD matrices of the elements within the system, as shown by many textbooks [12-14].

Many scientific papers demonstrated their matrix-based 3D ray tracing with larger, say 4×4 [17-21], 5×5 [22], or 6×6 [23, 24], matrices, where in some special cases the 4×4 matrix of an optical element could be exploded into two 2×2 matrices to trace the two orthogonal components of a ray, respectively [17, 20]. When coming across a symmetric optical system, it was normally claimed that the system could be analyzed using the textbooks' paradigm 2×2 matrix approach [20, 21, 25]. The statement is true if the ray of interest is confined to a meridional plane. If not, the situation is no longer that simple and straightforward.

Without running into the hassle of dealing with the 4×4 or larger matrices, in this section we confirm that with symmetric optical components and under paraxial approximation, two sets of 2×2 ABCD matrices, each for a 2D subspace, can be used to describe the 3D ray propagation completely, even for a non-meridional ray. The guides for 3D ray tracing using 2×2 ABCD matrices are also described.

2.1 Refraction at a Spherical Surface

We first define the *z* axis as the optical axis. A paraxial ray hits a spherical surface *S* at a point (*x*, *y*). (The *z* coordinate is not explicitly written out here.) (See Fig. 1) The surface *S* is described by the following equation, where *R* is the radius of curvature of the spherical surface.

$$S: x^2 + y^2 + z^2 = R^2 \tag{1}$$

The normal vector $\vec{s}$ at this point (*x*, *y*) is then

$$\vec{s} = (\frac{x}{R}, \frac{y}{R}, \frac{z}{R}) \tag{2}$$

Under paraxial approximation, *z*/*R* is close to unity and *x*/*R* and *y*/*R* are far smaller than 1. Therefore, $\vec{s}$ can be further written as

$$\vec{s} = (\frac{x}{R}, \frac{y}{R}, 1) \tag{3}$$

and has a vector length of approximately 1, i.e., it can be reasonably considered as a normal unit vector.

The direction of the paraxial ray can be described by a vector

$$\vec{k} = (\alpha, \beta, -1), \tag{4}$$

where α and β are the slopes of the ray in the *x* and *y* directions, respectively (Fig. 1), and are both far smaller than 1. $\vec{k}$ can also be considered approximately as a unit vector.

The ray vector after passing through the surface becomes

$$\vec{k}' = (\alpha', \beta', -1) . \tag{5}$$

If the refractive indices of the media before and behind the surface are n and n', respectively, then by Snell's law the relationship between the above vectors is

$$n'(\vec{s} \times \vec{k}') = n(\vec{s} \times \vec{k}) . \tag{6}$$

Substituting equations (2) – (5) into equation (6), we obtain

$$n'(\frac{-y}{R} - \beta', \alpha' + \frac{x}{R}, \frac{\beta' x - \alpha' y}{R}) = n(\frac{-y}{R} - \beta, \alpha + \frac{x}{R}, \frac{\beta x - \alpha y}{R}) \tag{7}$$

Equating the x and y components respectively, we find

$$\alpha' = (\frac{n - n'}{n'})\frac{x}{R} + \frac{n}{n'}\alpha \tag{8}$$

$$\beta' = (\frac{n - n'}{n'})\frac{y}{R} + \frac{n}{n'}\beta . \tag{9}$$

This, along with the fact that the position of the ray at the surface does not change after refraction, i.e., $x' = x$ and $y' = y$, leads to the following two relations that involve 2×2 matrices and ray vectors (position-slope pairs):

$$\begin{pmatrix} x' \\ \alpha' \end{pmatrix} = \begin{pmatrix} 1 & 0 \\ \frac{n - n'}{R \cdot n'} & \frac{n}{n'} \end{pmatrix} \cdot \begin{pmatrix} x \\ \alpha \end{pmatrix} \tag{10}$$

$$\begin{pmatrix} y' \\ \beta' \end{pmatrix} = \begin{pmatrix} 1 & 0 \\ \frac{n - n'}{R \cdot n'} & \frac{n}{n'} \end{pmatrix} \cdot \begin{pmatrix} y \\ \beta \end{pmatrix} \tag{11}$$

The two 2×2 matrices above, for the ray's x and y components respectively, are identical to that used for a spherical surface in a 2D space. Therefore, to describe the 3D ray propagation through a spherical surface completely, we can first decompose the ray into x and y components,

find their corresponding ray vectors (x, α) and (y, β), and treat each component as we normally do in a 2D space. This is also true for a plane surface as a plane is obtained with $R \rightarrow \infty$.

It should be noted that the above derivation, in which R is positive, considers a ray hitting a convex surface. However, we can find that when a concave surface is considered, all the equations, Eqs. (2)-(11) still stand but with R taken as negative.

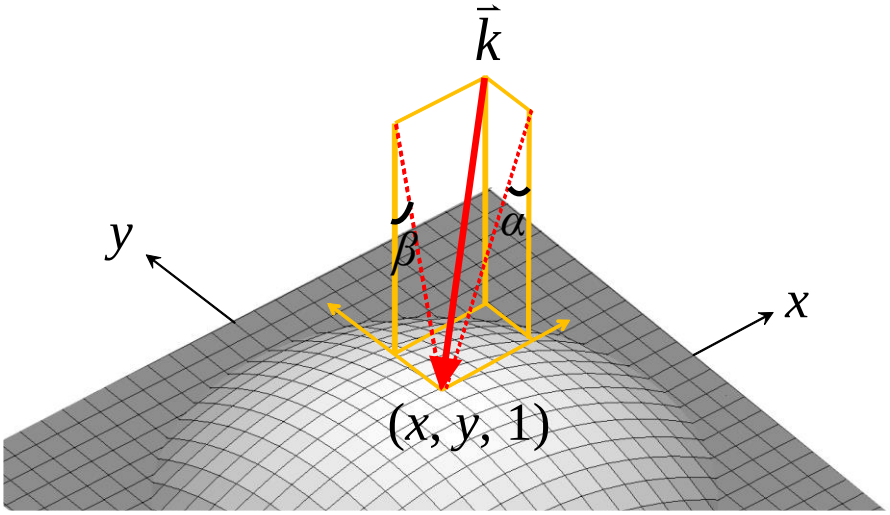

Fig. 1 Paraxial ray hitting a spherical surface in a 3D space

2.2 Reflection off a Spherical Surface

Similar derivation can be made in the case of reflection off a spherical surface with a radius of curvature R, where R is positive for a concave surface and negative for a convex one. A paraxial ray hits the reflecting surface at location (x, y), where the normal vector $\vec{s}$ is

$$\vec{s} = (\frac{x}{R}, \frac{y}{R}, 1) \tag{12}$$

Again, the direction of the paraxial ray can be described by a vector

$$\vec{k} = (\alpha, \beta, 1) \tag{13}$$

and the ray vector after reflection becomes

$$\vec{k}' = (\alpha', \beta', -1) . \tag{14}$$

By Snell's law and under paraxial approximation, the following relation stands as shown in Fig. 2 [26].

$$\vec{k} - \vec{s} = \vec{k}' + \vec{s} \tag{15}$$

Equating the *x* and *y* components on both sides, respectively, we obtain

$$\alpha' = \alpha - \frac{2x}{R} \tag{16}$$

$$\beta' = \beta - \frac{2y}{R} \tag{17}$$

Moreover, the reflected ray's position on the surface remains the same, i.e.

$$x' = x \tag{18}$$

$$y' = y \tag{19}$$

Combining Eqs. (16) with (18) and (17) with (19), the following two equations relating the input and output ray vectors are derived.

$$\begin{pmatrix} x' \\ \alpha' \end{pmatrix} = \begin{pmatrix} 1 & 0 \\ \frac{-2}{R} & 1 \end{pmatrix} \cdot \begin{pmatrix} x \\ \alpha \end{pmatrix} \tag{20}$$

$$\begin{pmatrix} y' \\ \beta' \end{pmatrix} = \begin{pmatrix} 1 & 0 \\ \frac{-2}{R} & 1 \end{pmatrix} \cdot \begin{pmatrix} y \\ \beta \end{pmatrix} \tag{21}$$

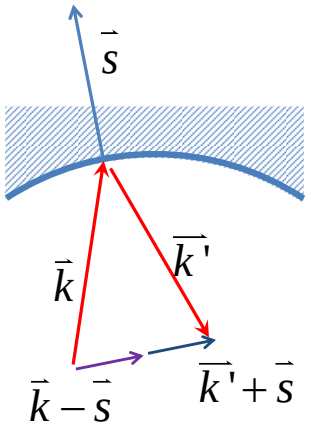

Fig. 2 Paraxial ray reflecting off a spherical surface in a 3D space – cross-sectional view. The relation among $\vec{s}$, $\vec{k}$, and $\vec{k}'$ is depicted.

Like the case of refraction, the two 2×2 matrices above, for the ray's *x* and *y* components respectively, are identical to that used for reflection in a 2D space. Therefore, to completely describe the ray reflection off a spherical surface in a 3D space, we can handle the ray vectors of the x and *y* components in the same way we normally do for a ray vector in the 2D space.

2.3 Propagation

For a ray simply propagating in a medium, the same conclusion can be drawn, i.e.,

$$\begin{pmatrix} 1 & d \\ 0 & 1 \end{pmatrix}$$

can be used to find the ray vectors of the *x* and *y* components after propagating for a distance *d*.

The conclusion can extendedly apply to a refractive optical element like lens, as ray propagation through such an element involves passing plane and/or spherical surfaces and propagating in medium which the optical element is made of.

3. Presimulation Analysis

With the guides derived in Section 2, we build models to simulate the micro cat's eye structure shown in Fig. 3. The cat's eye consists of a front-side focusing unit and a back-side reflecting unit, separated by an air gap, a filling material (refractive index = n_{fill}), or a smart film if tuning is required [8]. The front-side focusing unit is composed of a microlens (refractive index = $n_{lens,\,1}$) and a transparent carrier substrate (refractive index = $n_{substrate,\,1}$). The back-side reflecting unit bears the same structure except that the side with the microlens (refractive index = $n_{lens,\,2}$) is coated with reflective metal to form a concave mirror. Neglecting the thicknesses of the microlenses, the ABCD matrices of all elements shown in Fig. 3 are listed as follows.

$$Lens = \begin{pmatrix} 1 & 0 \\ \dfrac{n_{air} - n_{lens,1}}{n_{air} R_1} & 1 \end{pmatrix} \quad Mirror = \begin{pmatrix} 1 & 0 \\ \dfrac{-2n_{lens,\,2}}{n_{air} R_2} & 1 \end{pmatrix}$$

$$Gap = \begin{pmatrix} 1 & \dfrac{n_{air} d_{fill}}{n_{fill}} \\ 0 & 1 \end{pmatrix} \quad Substrate_1 = \begin{pmatrix} 1 & \dfrac{n_{air} d_1}{n_{substrate,1}} \\ 0 & 1 \end{pmatrix} \quad Substrate_2 = \begin{pmatrix} 1 & \dfrac{n_{air} d_2}{n_{substrate,\,2}} \\ 0 & 1 \end{pmatrix}$$

(Refer to Fig. 3 for the meanings of the symbols above.)

The ray transfer matrix of the entire cat's eye is then

$$Lens \cdot Substrate_1 \cdot Gap \cdot Substrate_2 \cdot Mirror \cdot Substrate_2 \cdot Gap \cdot Substrate_1 \cdot Lens .$$

The simulation is done using MATLAB and results will be compared to those obtained by FRED, a commercial ray tracing software [27].

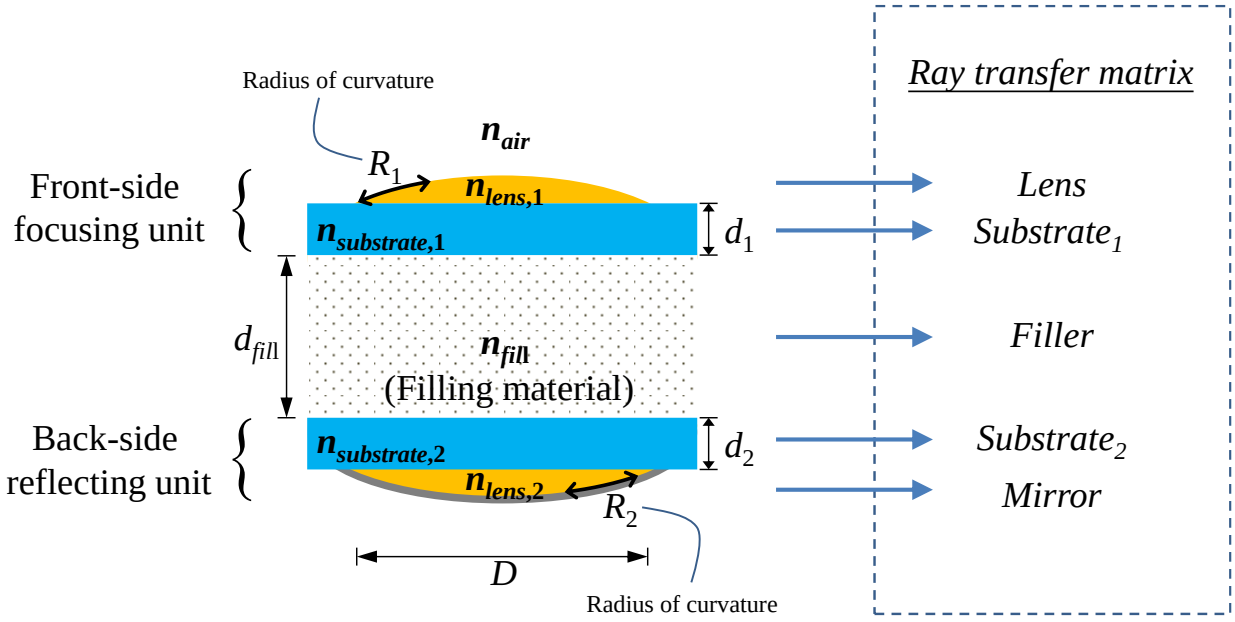

Fig. 3 Cat's eye structure presented in [8]

Before showing the simulation results, we first discuss the ideal cat's eye. An ideal cat's eye retroreflector should satisfy the following conditions: (1) the reflecting surface of the back-side unit should be situated right at the focal point of a collimated bundle of incident rays; (2) the focused ray bundle should hit the reflecting surface normally no matter what its angle of incidence is at the entrance aperture. To meet these requirements, the relations below have to hold.

$$d_{fill} = \frac{R_1 \cdot n_{fill}}{n_{lens,1} - n_{air}} - \frac{d_1 \cdot n_{fill}}{n_{substrat,1}} - \frac{d_2 \cdot n_{fill}}{n_{substrat,2}} \tag{22}$$

$$R_2 = \frac{R_1 \cdot n_{lens,2}}{n_{lens,1} - n_{air}} \tag{23}$$

The two equations are obtained by simply employing geometrical optics and ignoring the microlenses' thicknesses but without using the ABCD matrix approach. With the equations being satisfied, the *x*- and *y*-component ABCD matrices of the entire cat's eye are both simplified to

$$\begin{pmatrix} -1 & 0 \\ 0 & -1 \end{pmatrix} \tag{24}$$

This means a ray exits the aperture from a location right opposite to where it enters the cat's eye, and its incoming and outgoing paths are parallel. With a device structure exhibiting rotational symmetry around the optical axis, this implies that as long as a ray is able to hit the back-side concave reflective surface, it is guaranteed to exit through the aperture of cat's eye. It is also worth noting that Eq. (22) itself yields A = -1, C = 0, and D = -1, and adding in Eq. (23) leads to B = 0.

The acceptance angle of this ideal cat's eye can be estimated as follows. An optical ray bundle is retroreflected as long as it is focused onto the concave reflective surface. As the incident angle to the cat's eye aperture increases, the focal point moves toward the edge of the concave mirror. Therefore, the acceptance angle approximates to the angle of incidence beyond which the focal point is no longer within the reflecting area of the back-side mirror; the angle is

$$\theta = \pm \frac{D\left(n_{Lens,1} - n_{air}\right)}{2n_{air}R_1} \tag{25}$$

where *D* is the diameter of the concave mirror.

4. Simulation Results

In our simulations, the diameters of the front-side lens and back-side concave mirror are both 300 μm, which is therefore the size of the cat's eye aperture. A square grid of optical rays is incident on the cat's eye as shown in Fig. 4; 8000 of them are covered by the cat's eye entrance aperture and contribute to the power received by the cat's eye. Any ray that hits the back-side

concave mirror and exits through the same aperture will be counted toward the power reflected by the cat's eye device. Our models are able to calculate the retroreflection efficiency, acceptance angle, angular deviation of the retroreflected beam from the incoming path, and beam divergence.

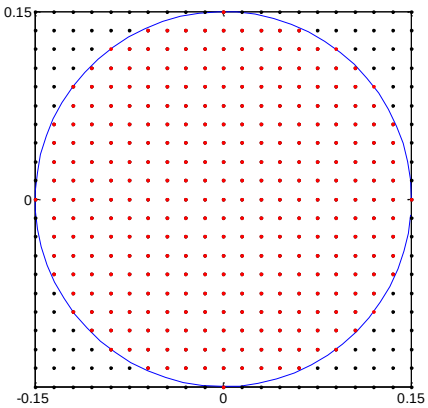

Fig. 4 Schematic drawing - a square grid of optical rays is incident on the cat's eye.

A. Verification of Validity of the Proposed Matrix-based 3-D Ray Tracing Approach

We compare our modeling approach with two other methods, FRED (commercial ray tracing software) simulation and traditional 2D ABCD matrix calculation, to verify its validity. The cat's eye structures reported in [8] are analyzed and the results obtained with FRED are used as the standards. It is worth noting that the structures are not ideal cat's eyes. In the simulations, the transmittances at the interfaces and the reflectivity of the back-side mirror are both set as 100%; the absorption within materials is not considered. The device dimensions are R_1 = 0.495 mm, R_2 = 0.801 mm, $d_1 = d_2$ = 0.15 mm, and d_{fill} = 0.45 mm while the indices of refraction are $n_{lens,\,1} = n_{lens,\,2}$ = 1.64, $n_{substrat,\,1} = n_{substrat,\,2}$ = 1.5, and $n_{fill} = n_{air}$ = 1 (i.e. units separated by an air gap).

For the cat's eye structure without a lateral *x* offset (misalignment) between the front and back units, all three simulation methods demonstrate a steep efficiency drop around the incident angle of 12.5° [Fig. 5(a)]. However, the traditional 2D ABCD matrix method yields a significantly higher efficiency than that obtained by FRED. On the other hand, the curve calculated by the proposed matrix-based 3D approach in this paper well matches that from FRED; it deviates slightly from the FRED curve at large angles where paraxial approximation is less valid.

Introducing a lateral *x* offset (misalignment) of -0.02 mm, all methods show that the incident angle where maximum efficiency occurs shifts to ~ 5° [Fig. 5(a)]. Again, similar trends are observed: the traditional 2D ABCD matrix approach significantly overestimates the efficiency; the curve calculated by our proposed method deviates slightly from the FRED curve at large angles.

When a lateral offset along the *y* direction (-0.02 mm) is introduced, the traditional 2D ABCD matrix method can no longer be used. The results from the proposed 3D approach and FRED match well [Fig. 5(c)).

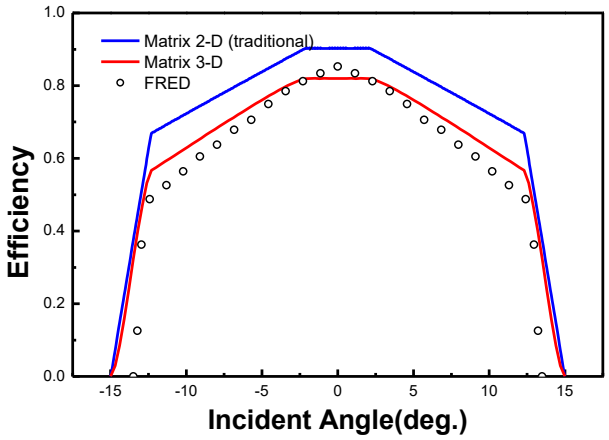

(a)

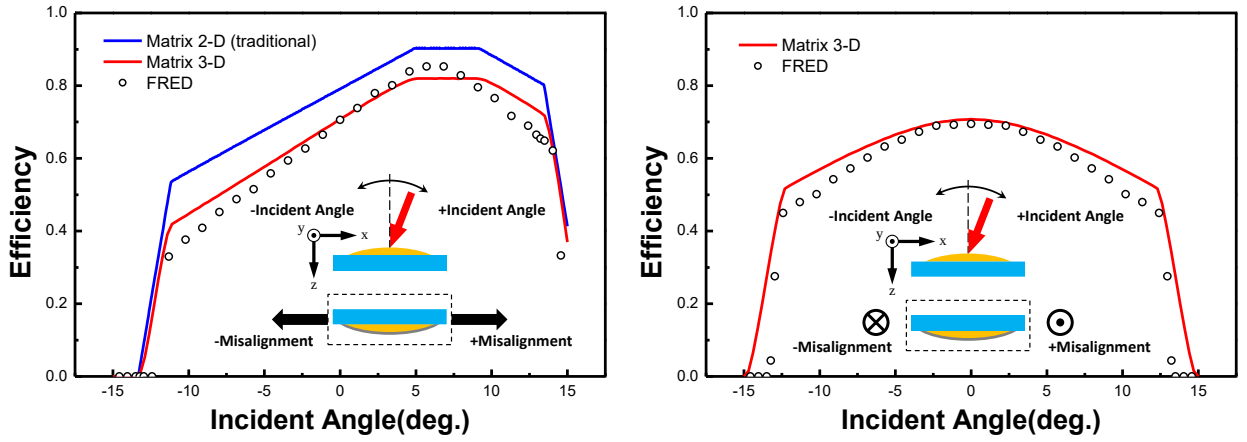

(b) (c)

Fig. 5 Comparison of the efficiency-incident angle relations among different simulation methods, when there is (a) no lateral offset/misalignment, (b) an *x* offset/misalignment of -0.02 mm, or (c) a *y* offset/misalignment of -0.02 mm.

As shown above, a lateral *x* offset in effect tilts the FOV of the cat's eye; more results from our 3D simulations are shown in Fig. 6(a). A *y* offset, on the other hand, does not tilt the FOV as the *x* offset does; however, the efficiency drops as the offset increases [Fig. 6(b)].

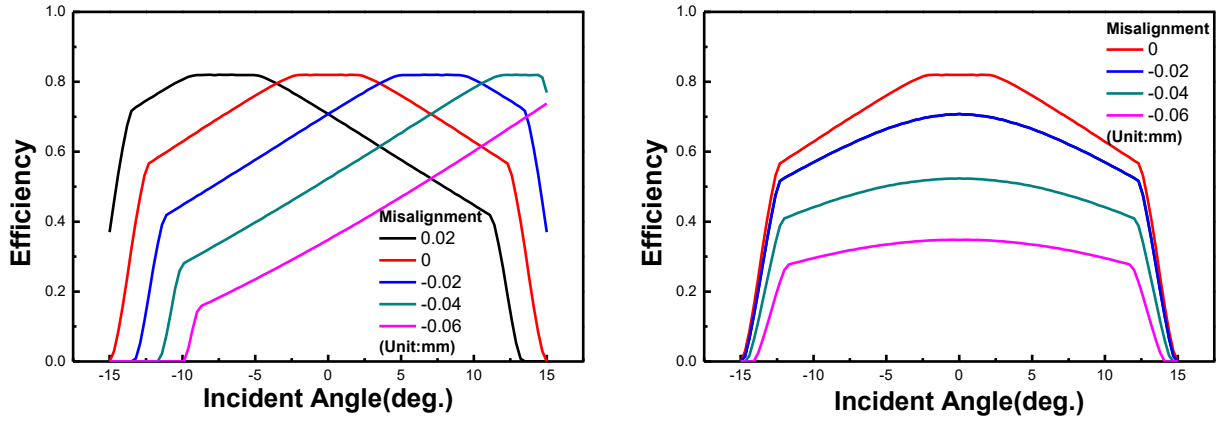

(a) (b)

Fig. 6 Retroreflection efficiency versus incident angle for (a) different *x* offsets (misalignments) and (b) different *y* offsets. Please refer to the insets of Fig. 5 for the lateral shift's direction of a certain misalignment amount.

B. Ideal Cat's Eye

We then model an ideal cat's eye. The dimensions of this cat's eye are R_1 = 0.495 mm, R_2 = 1.268 mm, d_1 = d_2 = 0.15 mm, and d_{fill} = 0.573 mm while the refractive indices are $n_{lens,\,1}$ = $n_{lens,2}$ = 1.64, $n_{substrat,\,1}$ = $n_{substrat,\,2}$ = 1.5, and n_{fill} = n_{air} = 1 (i.e. units separated by an air gap). These values satisfy Eq. (22) and (23), and all of them, except R_2 and d, are the same as those in Section 4.A. The result is plotted in Fig. 7, where that obtained by FRED is also shown for comparison. According to our model, perfect retroreflection with 100% efficiency occurs as long as the angle of incidence falls within the FOV defined by Eq. (25).

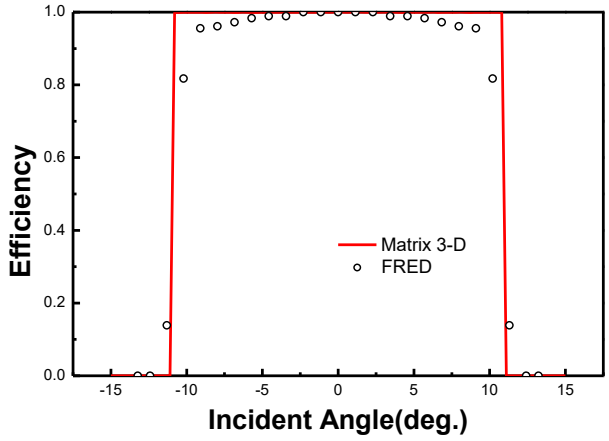

Fig. 7 Simulation results of efficiency versus incident angle for an ideal cat' eye, calculated by our matrix-based 3D technique and FRED, respectively.

C. Deviation from an Ideal Cat's Eye

There always exists fabrication inaccuracies or errors which make it impossible to manufacture an ideal cat's eye. For example, lateral offsets/misalignement in the x and y directions between units can occur during the assembly step. The radius of curvature of the focusing lens or concave mirror most likely deviates from the targeted value if it is made using

the thermal reflow process. The gap between the units may also be off the designed size. To learn the effects of these fabrication inaccuracies, in this section we analyze cat's eyes which deviate from the ideal one.

First we take into account the lateral offset/misalignment. Consider that a lateral x offset/misalignment is introduced between the front-side and back-side units of the ideal cat's eye, making it not ideal anymore. As the offset/misalignment increases, the FOV shifts and the maximum efficiency drops [Fig. 8(a)]. A lateral y offset does not shift the FOV but does lower the efficiency [Fig. 8(a)].

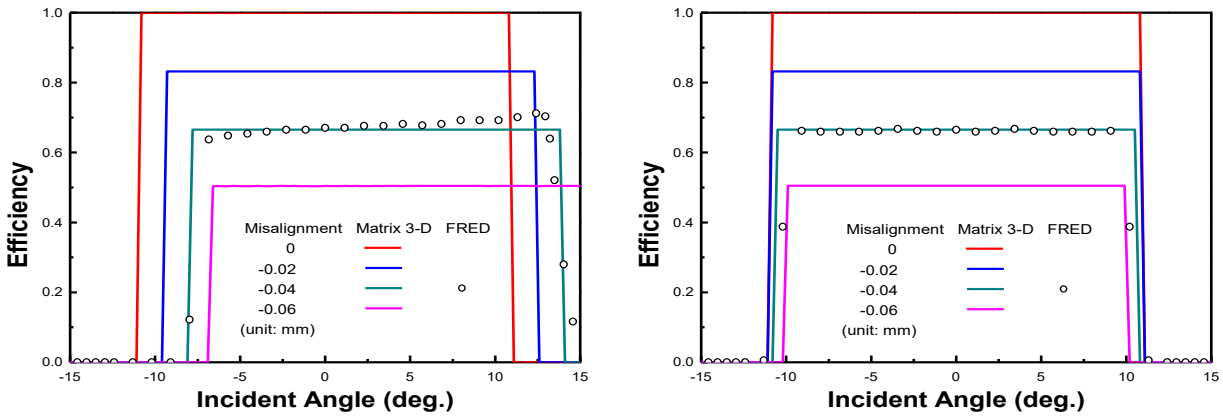

(a) (b)

Fig. 8 Efficiency versus incident angle when a lateral (a) x or (b) y offset (misalignment) is introduced, making the cat's eye not ideal anymore.

Second, we consider the deviation of the radius of curvature and gap. Given all the indices of refraction and the substrate thicknesses d_1 and d_2, the values of R_1, R_2, and d_{fill} have to satisfy Eq. (22) and (23) for a cat's eye retro-reflector to be ideal. However, in a fabricated device these three dimensions are all likely to deviate from their targeted values, as mentioned previously. No matter what R_1, R_2, and d_{fill} turn out to be after the fabrication process, we can always substitute the value of R_1 of the final device into Eq. (22) and (23), and find the corresponding ideal values

of R_2 and d_{fill}. Then, we can see how R_2 and d_{fill} of the real device deviate from these ideal values, and evaluate the effect of these deviations. Given $n_{lens,\,1} = n_{lens,\,2} = 1.64$, $n_{substrat,\,1} = n_{substrat,\,2} = 1.5$, and $n_{fill} = n_{air} = 1$ (i.e. units separated by an air gap) in the following discussion, we again take R_1 = 0.495 mm; the ideal values for the gap between the units (d_{fill}) and radius of curvature (R_2) are then 0.573 mm (later denoted by d for convenience) and 1.268 mm (later denoted by R for convenience), respectively, according to Eq. (22) and (23). Fig. 9 shows how the relation of effciency versus incident angle varies with R_2 if the gap d_{fill} is fixed at d. It can be seen that when R_2 is off the ideal value R, the efficiency drops more at a larger incident angle. Also, the amount of this efficiency drop is proportional to $|1/R_2\text{-}1/R|$

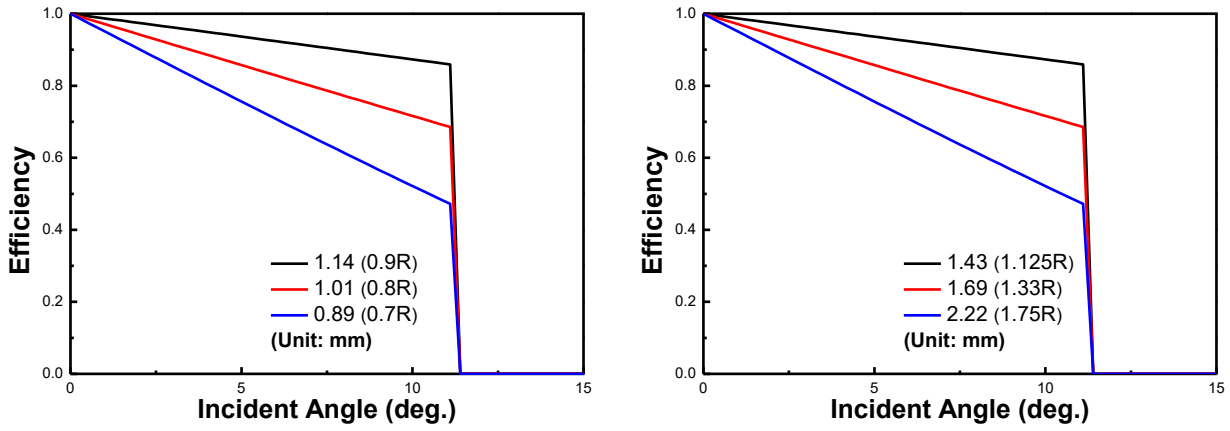

(a) (b)

Fig. 9 Effciency versus incident angle when (a) $R_2 < R$ (1.268 mm) and (b) $R_2 > R$ (1.268 mm)

When d_{fill} moves away from the ideal value d, not only does the efficiency change, but the reflected beam also diverges and deviates from the ideal retro-reflection direction which is parallel to the incoming path. Fig. 10 shows how the divergence angle (half angle) and angular deviation vary with d_{fill}, under three different R_2 values and an incident angle of 5°. The efficiency is also shown.

In the case with the ideal value R (1.268 mm) for R_2 [Fig. 10(a)], the divergence angle and angular deviation are both 0 when the gap size is d (0.573 mm), the ideal value. As the gap size shifts away from the ideal value, both the divergence angle and angular deviation increase. As shown in Fig. 10(a), the angular deviatoin is much less sensitive to the gap change than the beam divergence is in this case. It is observed that below the gap size of 0.47 mm the efficiency actually rises as the gap size decreases. This is because a shorter propagation distance between the units ensures that more light rays reflected from the back-side mirror pass through the entrance aperture and contribute to the efficiency. The results from FRED are also shown simply for comparison. The slight difference between the divergence results of our model and FRED may be due to the neglect of the lenses' thicknesses in our model.

The results of $R_2 = 0.8R$ and $R_2 = \infty$ (plane mirror) are shown in Fig. 10(b) and 10(c), respectively. Compared to the mirror with an ideal radius of curvature $R_2 = R$, the plane mirror makes the angular deviation more susceptible to gap change, but on the other hand, causes less beam divergence.

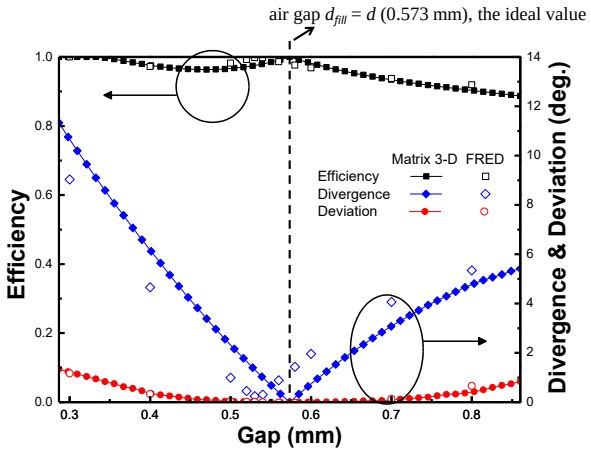

(a)

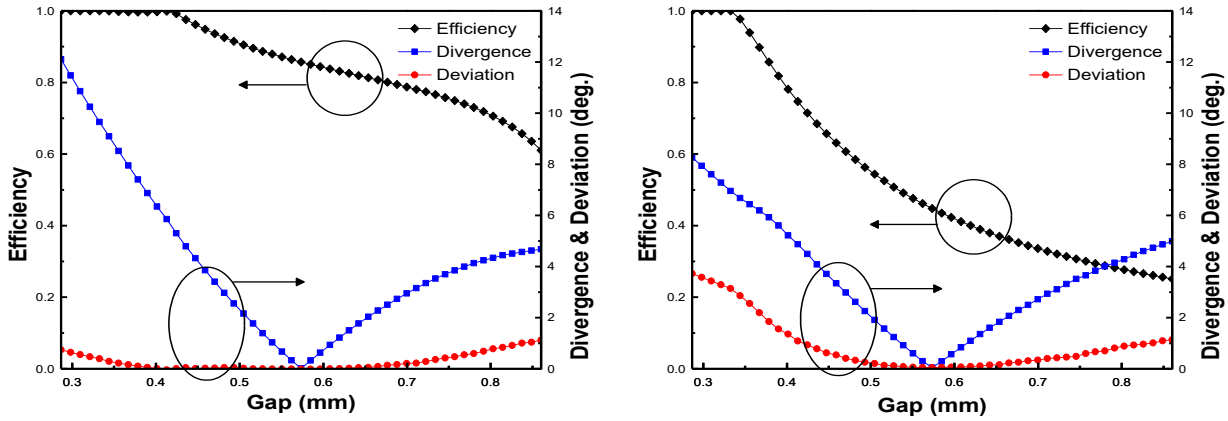

(b) (c)

Fig. 10 Efficiency, divergence angle, and angular deviatoin versus the air gap d_{fill} for three different R_2 values, (a) R, (b) 0.8R, and (c) ∞. The incident angle is 5°.

Fig. 11 shows the efficiency, divergence angle, and angular deviation versus angle of incidence for several cat's eye structures with different d_{fill} and R_2. The characteristics of the ideal cat's eye in Section 4.B and the cat's eye in Section 4.A are shown again in Fig. 11(e) and Fig. 11(j), respectively, for comparison.

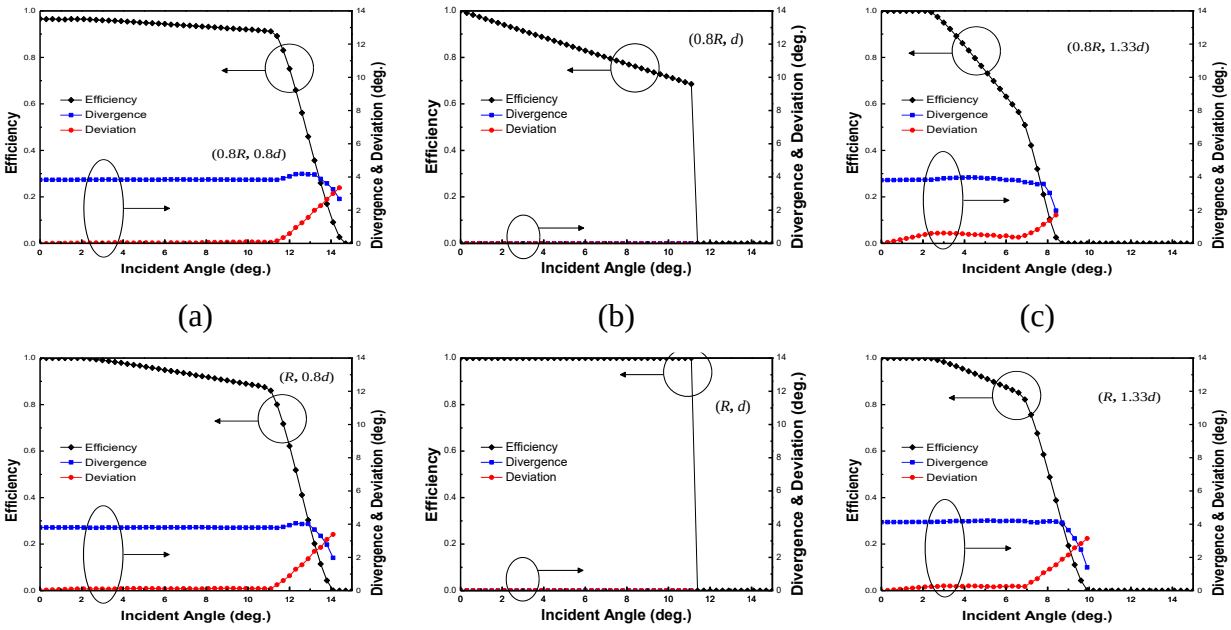

(a) (b) (c)

(d) (e) (f)

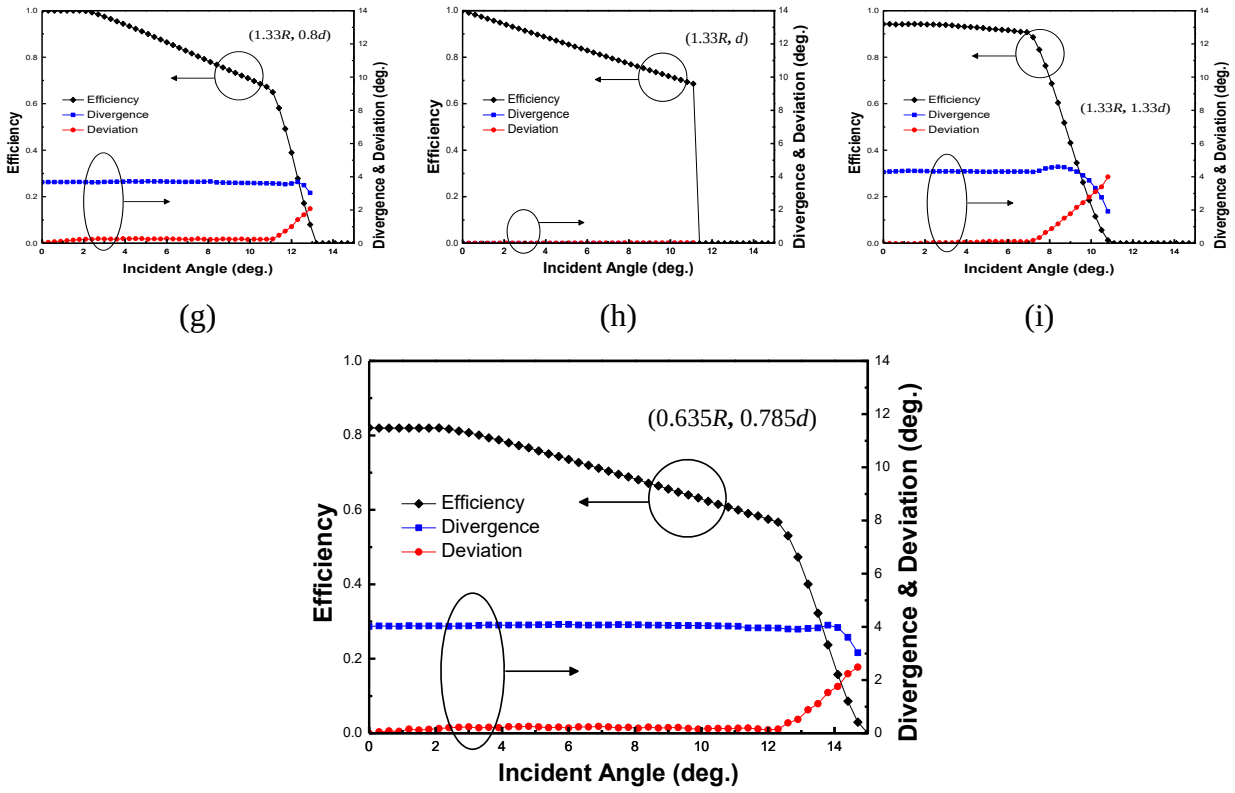

(g) (h) (i)

(j)

Fig. 11 Efficiency, divergence angle, and angular deviation versus angle of incidence, for several cat's eye structures with different (R_2, d_{fill}): (a) (0.8R, 0.8d), (b) (0.8R, d), (c) (0.8R, 1.33d), (d) (R, 0.8d), (e) (R, d), (f) (R, 1.33d), (g) (1.33R, 0.8d), (h) (1.33R, d), (i) (1.33R, 1.33d), and (j) (0.635R, 0.785d). The characteristics of the ideal cat's eye in Section 4.B and the cat's eye in Section 4.A are shown again in (e) and (j), respectively, for comparison.

Figure 12 shows the characteristics of non-ideal cat's eyes with specially selected values for (R_2, d_{fill}), which are (0.85R, 0.8d) and (1.2R, 1.27d), respectively. The efficiency-incident angle relations under different x misalignments are also shown. The efficiency-incident angle curves exhibit flat regions, where efficiency is 1, just as that of the ideal cat's eye. However, the retro-reflected beams are subjected to divergence of ~ 4°. In either device the FOV shifts and the efficiency drops as the offset/misalignment increases, just as in the ideal cat's eye.

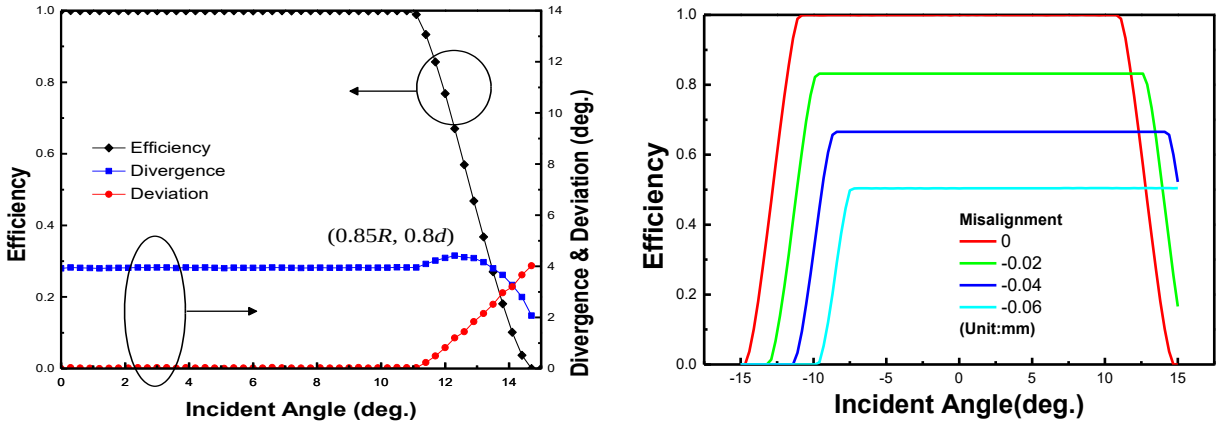

(a)

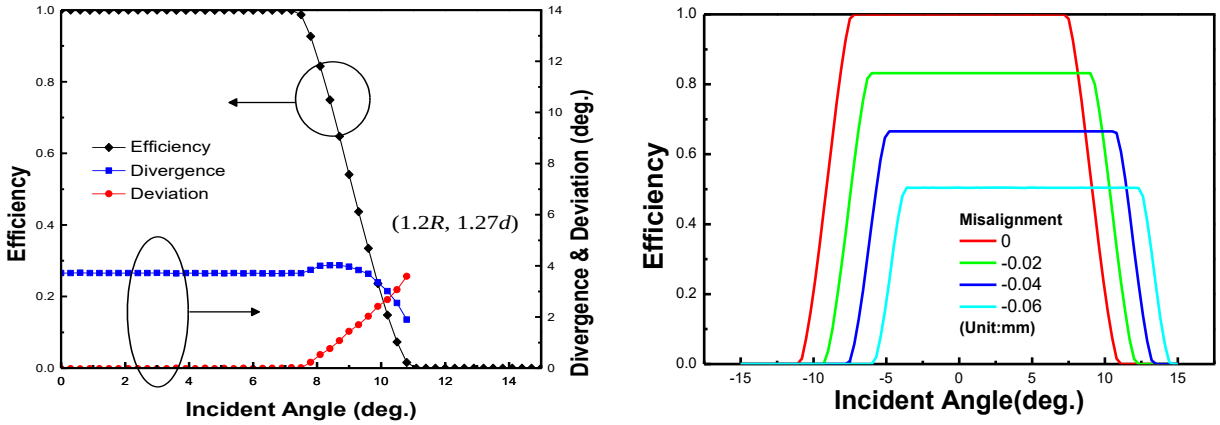

(b)

Fig. 12 Characteristics of nonideal cat's eyes with specially selected values for (R_2, d_{fill}), which are (a) (0.85R, 0.8d) and (b) (1.2R, 1.27d), respectively. The efficiency-incident angle relations under different x misalignments are also shown.

5. Conclusion

We develop a 3D ray tracing tool based on the ABCD ray transfer matrices to model cat's eye retroreflectors. Compared to commercial ray tracing software packages, our tool saves time and costs. The application of this matrix-based 3D ray tracing method can be further extended to other optical components.

The cat's eye performance, including the retroreflection efficiency, acceptance angle (i.e. FOV), beam divergence and deviation, is fully studied. Whether a cat's eye structure is optimal or not really depends on its application. For example, when it is used for traffic signs, a certain degree of reflected beam divergence is probably needed since the car's headlights and driver are separated by a meter or so. If the cat's eye is employed in a high-security/privacy optical ID tag, a limited acceptance angle (i.e. FOV) is preferred to avoid any bystander stealing the tag information with a proper light source and detector. The study in this paper not only develops a 3D-ray tracing tool, but also provides tips for finding the optimal cat's eye design for a certain application.

Acknowledgment

This work was supported by National Science Council of Taiwan under Grants NSC 99-2628-E-002-004, NSC 100-2628-E-002-002, and NSC 101-2221-E-002-056-MY3, and Excellent Research Projects of National Taiwan University, 10R80919-1. This article is reprinted from *Bing-jun Yang, Keng-hsing Chao, and Jui-che Tsai, "Modeling of micro cat's eye retroreflectors using a matrix-based three-dimensional ray tracing technique," Appl. Opt. 51, 6020-6030 (2012).*

References

1. http://www.reflexite.com/refl/americas/en/traffic-control.
2. W. S. Rabinovich, R. Mahon, H. R. Burris, G. C. Gilbreath, P. G. Goetz, C. I. Moore, M. F. Stell, M. J. Vilcheck, J. L. Witkowsky, L. Swingen, M. R. Suite, E. Oh, and J. Koplow, “Free space optical communications link at 1550 nm using multiple-quantum-well modulating retroreflectors in a marine environment,” Opt. Eng. 44, 56001-56012 (2005).
3. G. C. Gilbreath, W. S. Rabinovich, T. J. Meehan, M. J. Vilcheck, R. Mahon, R. Burris, M. Ferraro, I. Solkolsky, J. A. Vasquez, C. S. Bovais, K. Cochrell, K. C. Goins, R. Barbehenn, D. S. Katzer, K. Ikossi-Anas-tasiou, and M. J. Montes, “Large-aperture multiple quantum well modulating retroreflector for free-space optical data transfer on unmanned aerial vehicles,” Opt. Eng., vol. 40, pp. 1348–1356, July 2001.
4. P. G. Goetz, W. S. Rabinovich, R. Mahon, J. L. Murphy, M. S. Ferraro, W. R. Smith, B. B. Xu, H. R. Burris, C. I. Moore, and W. W. Schultz, "Modulating retro-reflector lasercom systems at the Naval Research Laboratory," in *The 2010 Military Communications Conference*, 2010, pp. 1601-1606.
5. J. C. Juarez, A. Dwivedi, A. Mammons, S. D. Jones, V. Weerackody, and R. A. Nichols, "Free-space optical communications for next-generation military networks," *Communications Magazine, IEEE,* vol. 44, pp. 46-51, 2006.
6. D. J. Hayes, "Cat's eye retro-reflector array coding device and method of fabrication," US Patent, US 7,152,984 B1, 2006.
7. K. H. Chao, C. D. Liao, and J. C. Tsai, "Array of cat's eye retro-reflectors with modulability for an optical identification system," in *2010 International Conference on Optical MEMS & Nanophotonics*, 2010, pp. 7-8.

8. K. H. Chao, C. D. Liao, B. J. Yang, and J. C. Tsai, "Fabrication and characterization of a micro tunable cat's eye retro-reflector," *Optics Communications,* Vol. 284, pp. 5221-5224, Oct. 2011.
9. X. Zhu, V. S. Hsu, and J. M. Kahn, "Optical modeling of MEMS corner cube retroreflectors with misalignment and nonflatness," *IEEE Journal of Selected Topics in Quantum Electronics,* vol. 8, pp. 26-32, 2002.
10. V. A. Handerek and L. C. Laycock ,"Feasibility of retroreflective free-space optical communication using retroreflectors with very wide field of view", *Proc. SPIE*, vol. 5614, pp.1-9, 2004
11. P. G. Goetz, W. S. Rabinovich, R. Mahon, L. Swingen, G. C. Gilbreath, J. L. Murphy, H. R. Burris, and M. F. Stell, "Practical considerations of retroreflector choice in modulating retroreflector systems," in *2005 Digest of the LEOS Summer Topical Meetings,* ,pp. 49-50, 2005.
12. E. Hecht, "6.2 Analytical Ray Tracing," in *Optics*, 4th Ed. Addison-Wesley, 2002, pp. 246-253.
13. A. Gerrard and J. M. Burch, "Matrix methods in paraxial optics," in *Introduction to Matrix Methods in Optics*, New York: Dover, 1994, pp. 24-75.
14. H. A. Haus, "5.5 The ABCD Matrix in Ray Optics," in *Waves and Fields in Optoelectronics*, Englewood Cliffs, NJ: Prentice-Hall, 1984, pp. 132-136.
15. A. Nussbaum, "Modernizing the teaching of advanced geometric optics," in Proc. SPIE Vol. 1603, pp. 389-400, 1992.
16. J. J. Snyder, "Paraxial ray analysis of a cat's-eye retroreflector," *Appl. Opt.,* vol. 14, pp. 1825-1828, 1975.

17. H. H. Arsenault, “A matrix representation for non-symmetrical optical systems,” *J. Optics (Paris)*, vol. 11, no 2. pp. 87-01, 1980.
18. B. Macukow and H. H. Arsenault, “Matrix decompositions for nonsymmetrical optical systems,” *J. Opt. Soc. Am.*, Vol. 73, No. 10, pp. 1360-1366, October 1983.
19. B. Lu, S. Xu, Y. Hu, and B. Cai, “Matrix representation of three-dimensional astigmatic resonators,” *Optical and Quantum Electronics*, Vol. 24, pp. 619-630, 1992.
20. I. Moreno, C. Ferreira, and M. M. Sanchez-Lopez, “Ray matrix analysis of anamorphic fractional Fourier systems,” *J. Opt. A: Pure Appl. Opt.*, Vol, 8, pp. 427–435, 2006.
21. K. Chen, H. Yang, L. Sun, and G. Jin “Astigmatism analysis by matrix methods in White Cells,” *Proc. of SPIE*, Vol. 7156, 71560G, 2009.
22. W. F. Harris, “Paraxial ray tracing through noncoaxial astigmatic optical systems, and a 5 × 5 augmented system matrix,” *Optometry and Vision Science*, Vol. 71, No. 4, pp. 282-285, 1994.
23. P. D. Lin and C. K. Sung “Matrix-based paraxial skew ray-tracing in 3D systems with non-coplanar optical axis,” *Optik*, Vol. 117, pp. 329–340, 2006.
24. P.-D. Lin and C.-C. Hsueh, “6 × 6 matrix formalism of optical elements for modeling and analyzing 3D optical systems,” *Appl. Phys. B,* Vol. 97, pp. 135–143, 2009.
25. H. H. Arsenault and B. Macukow, “Factorization of the transfer matrix for symmetrical optical systems,” *J. Opt. Soc. Am.*, Vol. 73, No. 10, pp. 1350-1359, October 1983.
26. D. S. Goodman, "1.8 Refraction and reflection at interfaces between homogeneous media," in *Handbook of Optics, Volume 1, Geometrical and Physical Optics, Polarized Light, Components And Instruments*, 3rd Ed., Editor-in-Chief: M. Bass, New York: McGraw-Hill, 2010, pp. 1.23-1.26.
27. http://www.photonengr.com/software/.